Construction of First Principle Based Adiabatic and Diabatic Hamiltonian for TiO_6^{8-} unit of $BaTiO_3$ Crystal: Photoemission Spectra and Ferroelectricity

Mantu Kumar Sah[a], Soumya Mukherjee[a,b], Satyam Ravi[c] and Satrajit Adhikari[a,*]

[a]School of Chemical Sciences,

Indian Association for the Cultivation of Science, Jadavpur, Kolkata - 700032, India

[b]Department of Chemistry, MANIT, Bhopal, India

[c]School of Advanced Sciences, VIT Bhopal University, Bhopal, India

June 13, 2025

Electronic Supplementary Information

*Author to whom correspondence should be addressed: e-mail: pcsa@iacs.res.in

S1 Conditions for the JT and PJT Interactions

While exploring the conditions to understand the properties related to the distortions of TiO_6^{8-} unit of $BaTiO_3$ crystal, it appears that the vibrational modes (t_{2g} and t_{1u}) are responsible for Jahn-Teller (JT) and pseudo Jahn-Teller (PJT) interactions. On the other hand, the Ti^{4+} ion of TiO_6^{8-} unit having a d^0 electronic configuration leads to a non-degenerate ground state (A_{1g}), whereas the first excited state is triply degenerate (T_{1u}). The JT and PJT effects originate due to the coupling of electronic state with vibrational modes of appropriate symmetry. In other words, the direct product of irreducible representations for the electronic state and the vibrational mode contains the totally symmetric representation (A_{1g}). The JT distortion takes place between $^1T_{1u}$ states via t_{2g} normal modes:

$$A_{1g} \in t_{2g} \otimes [(T_{1u})^2] \equiv g \otimes u \otimes u,$$

whereas the PJT effect involves the coupling between the non-degenerate ground state (A_{1g}) and an excited state (T_{1u}) via vibrational modes (t_{1u}):

$$A_{1g} \in t_{1u} \otimes [A_{1g} \otimes T_{1u}] \equiv u \otimes g \otimes u.$$

Though our calculations reveal that the JT distortion due to interaction of t_{2g} normal modes with T_{1u} electronic states is negligibly small, the PJT stabilization for the coupling of t_{1u} modes with A_{1g} and $^1T_{1u}$ electronic states is significant. Moreover, *ab initio* calculation along other u-symmetric normal modes (t_{2u} and other set of t_{1u}) yield approximately the same stabilization energy (-0.65 eV) and thereby, one representative set of u-symmetric normal modes is chosen for the present calculation. This selection simplifies the calculation as predicted before[1] to depict the effect of PJT stabilization on photoemission spectra and ferroelectric properties.

S2 Adiabatic to Diabatic Transformation Equation: Curl Condition

In adiabatic Representation, the kinetically coupled SE can be written as:

$$-\frac{\hbar^2}{2}\left(\vec{\nabla}_R + \vec{\tau}\right)^2 \psi^{ad} + (U - E)\psi^{ad} = 0. \tag{S1}$$

Using the following transformation:

$$\psi^{ad} = A\psi^{d}, \tag{S2}$$

with ψ^{ad} and ψ^{d} as adiabatic and diabatic nuclear wavefunctions, respectively and 'A' being the adiabatic-to-diabatic transformation matrix, Eq. S1 turns into:

$$-\frac{\hbar^2}{2}\left(\vec{\nabla}_R + \vec{\tau}\right)^2 A\psi^{d} + (U-E)A\psi^{d} = 0, \tag{S3}$$

which appears as:

$$\begin{aligned} -\frac{\hbar^2}{2}\Big[A\nabla_R^2\psi^{d} + 2(\vec{\nabla}_R A + \vec{\tau}A)\cdot\vec{\nabla}_R\psi^{d} \;\; &+ \;\; \Big\{(\vec{\tau}+\vec{\nabla}_R)\cdot(\vec{\nabla}_R A + \vec{\tau}A)\Big\}\psi^{d}\Big]A\psi^{d} \\ &+ \;\; (U-E)A\psi^{d} = 0. \end{aligned} \tag{S4}$$

If the following constrain is imposed,

$$\vec{\nabla}_R A + \vec{\tau}A = 0, \tag{S5}$$

Eq. S4 reduces to the form as given below:

$$-\frac{\hbar^2}{2}A\nabla_R^2\psi^{d} + (U-E)A\psi^{d} = 0. \tag{S6}$$

On the other hand, when Eq. S5 is left multiplied by $A^\dagger$ and the daggered (†) of Eq. S5 is right multiplied by A, we obtain:

$$A^\dagger\vec{\nabla}_R A + A^\dagger\vec{\tau}A = 0, \tag{S7a}$$

$$(\vec{\nabla}_R A^\dagger)A - A^\dagger\vec{\tau}A = 0, \tag{S7b}$$

and then, on adding Eqs. S7a and S7b, we obtain:

$$\begin{aligned} A^\dagger\vec{\nabla}_R A + (\vec{\nabla}_R A^\dagger)A &= 0, \\ \Rightarrow \vec{\nabla}_R(A^\dagger A) &= 0, \\ \Rightarrow A^\dagger A &= \text{const}, \end{aligned} \tag{S8}$$

which defines A is an orthogonal matrix.

Therefore, we left multiply Eq. S6 by $A^\dagger$ and obtain the diabatic representation of SE:

$$-\frac{\hbar^2}{2}\nabla_R^2\psi^d + (W - E)\psi^d = 0, \tag{S9}$$

where

$$W = A^\dagger U A. \tag{S10}$$

The couplings between electronic states are incorporated within the potential energy matrix (W)[2].

While performing BBO-based diabatization of adiabatic PESs and NACTs, it is essential to verify whether the number of electronic states (N) within the relevant domain of nuclear space can be considered a "true" SHS for required numerical accuracy. The existence of such SHS can be assessed by evaluating the matrix elements of Curl Condition[3] associated with the NACTs as outlined below. For any pair of nuclear coordinates (p and q), the scalar form of Eq. S5 can be expressed as:

$$\nabla_p A + \tau_p A = 0, \tag{S11}$$

$$\nabla_q A + \tau_q A = 0, \tag{S12}$$

and by taking cross-derivatives to Eqs. S11 and S12, we obtain:

$$\nabla_q \nabla_p A + \Big(\frac{\partial}{\partial q}\tau_p\Big) A + \tau_p \frac{\partial}{\partial q} A = 0, \tag{S13a}$$

$$\nabla_p \nabla_q A + \Big(\frac{\partial}{\partial p}\tau_q\Big) A + \tau_q \frac{\partial}{\partial p} A = 0. \tag{S13b}$$

Since the matrix element of A are analytic functions of the nuclear coordinates (p and q) and $\nabla_q \nabla_p A = \nabla_p \nabla_q A$, we obtain the following Curl Condition:

$$\frac{\partial}{\partial p}\tau_q^{ij} - \frac{\partial}{\partial q}\tau_p^{ij} = (\tau_q \tau_p)_{ij} - (\tau_p \tau_q)_{ij}, \tag{S14}$$

where the matrix elements (analogous to Yang-Mills field) over $p - q$ plane are represented as:

$$F_{pq}^{ij} = \left[\frac{\partial}{\partial p}\tau_q^{ij} - \frac{\partial}{\partial q}\tau_p^{ij}\right] - \left[(\tau_q\tau_p)_{ij} - (\tau_p\tau_q)_{ij}\right] = Z_{pq}^{ij} - C_{pq}^{ij}. \tag{S15}$$

When the sub-space is complete, the magnitude of F_{pq}^{ij} should be zero (0) over the relevant domain of nuclear configuration space, ensuring that the non-removable component of the NACTs becomes negligibly small. If this condition is not satisfy for the chosen SHS, it becomes necessary to enlarge the sub-space in order to diabatize the SE in a "true" sense, achieving the desired level of accuracy.

S3 Explicit Expression of ADT Equations and NACTs for Four state ($N = 4$) sub-Hilbert space[4]

S3.1 ADT Equations

$$\begin{aligned}
\boldsymbol{\nabla}_R\Theta^{12} &= -\boldsymbol{\tau}^{12} - \sin\Theta^{12}\tan\Theta^{13}\boldsymbol{\tau}^{13} - \cos\Theta^{12}\tan\Theta^{13}\boldsymbol{\tau}^{23} - \sin\Theta^{12}\sec\Theta^{13}\tan\Theta^{14}\boldsymbol{\tau}^{14} - \cos\Theta^{12}\sec\Theta^{13}\tan\Theta^{14}\boldsymbol{\tau}^{24}\\
\boldsymbol{\nabla}_R\Theta^{13} &= -\cos\Theta^{12}\boldsymbol{\tau}^{13} + \sin\Theta^{12}\boldsymbol{\tau}^{23} - \cos\Theta^{12}\sin\Theta^{13}\tan\Theta^{14}\boldsymbol{\tau}^{14} + \sin\Theta^{12}\sin\Theta^{13}\tan\Theta^{14}\boldsymbol{\tau}^{24} - \cos\Theta^{13}\tan\Theta^{14}\boldsymbol{\tau}^{34}\\
\boldsymbol{\nabla}_R\Theta^{23} &= -\cos\Theta^{13}[\boldsymbol{\tau}^{13}\sin\Theta^{12}\sec^2\Theta^{13} + \cos\Theta^{23}\sec\Theta^{14}(\boldsymbol{\tau}^{34} - \boldsymbol{\tau}^{24}\sin\Theta^{12}\tan\Theta^{13})\tan\Theta^{24}\\
&\quad + \sin\Theta^{12}\sec\Theta^{13}\tan\Theta^{13}\boldsymbol{\tau}^{14}\tan\Theta^{14} + \sin\Theta^{23}\boldsymbol{\tau}^{14}\sec\Theta^{14}\tan\Theta^{24} + \cos\Theta^{12}\{\boldsymbol{\tau}^{23}\sec^2\Theta^{13}\\
&\quad + \tan\Theta^{13}\cos\Theta^{23}\boldsymbol{\tau}^{14}\sec\Theta^{14}\tan\Theta^{24} + \sec\Theta^{13}(\tan\Theta^{13}\boldsymbol{\tau}^{24}\tan\Theta^{14}\\
&\quad + \sin\Theta^{23}\boldsymbol{\tau}^{24}\sec\Theta^{14}\tan\Theta^{24})\}]\\
\boldsymbol{\nabla}_R\Theta^{14} &= -\cos\Theta^{12}\cos\Theta^{13}\boldsymbol{\tau}^{14} + \sin\Theta^{12}\cos\Theta^{13}\boldsymbol{\tau}^{24} + \sin\Theta^{13}\boldsymbol{\tau}^{34}\\
\boldsymbol{\nabla}_R\Theta^{24} &= \sin\Theta^{23}(-\sin\Theta^{12}\sin\Theta^{13}\boldsymbol{\tau}^{24}\sec\Theta^{14} + \cos\Theta^{13}\boldsymbol{\tau}^{34}\sec\Theta^{14}) - \sin\Theta^{12}\cos\Theta^{23}\boldsymbol{\tau}^{14}\sec\Theta^{14}\\
&\quad + \cos\Theta^{12}(\sin\Theta^{13}\sin\Theta^{23}\boldsymbol{\tau}^{14}\sec\Theta^{14} - \cos\Theta^{23}\boldsymbol{\tau}^{24}\sec\Theta^{14})\\
\boldsymbol{\nabla}_R\Theta^{34} &= \sin\Theta^{12}\{-\sin\Theta^{23}\boldsymbol{\tau}^{14}\sec\Theta^{14}\sec\Theta^{24} + \sin\Theta^{13}\cos\Theta^{23}\boldsymbol{\tau}^{24}\sec\Theta^{14}\sec\Theta^{24}\} + \cos\Theta^{12}[-\sec\Theta^{24}\\
&\quad \{\sin\Theta^{13}\cos\Theta^{23}\boldsymbol{\tau}^{14}\sec\Theta^{14} + \sin\Theta^{23}\boldsymbol{\tau}^{24}\sec\Theta^{14}\}] - \cos\Theta^{13}\cos\Theta^{23}\boldsymbol{\tau}^{34}\sec\Theta^{14}\sec\Theta^{24}
\end{aligned}$$

S3.2 NACTs

$$
\begin{aligned}
\boldsymbol{\tau^{12}} &= -\cos\Theta^{13}\cos\Theta^{23}\cos\Theta^{14}\cos\Theta^{24}\boldsymbol{\nabla}_R\Theta^{12} - \sin\Theta^{23}\cos\Theta^{14}\cos\Theta^{24}\boldsymbol{\nabla}_R\Theta^{13} - \sin\Theta^{24}\boldsymbol{\nabla}_R\Theta^{14} \\
\boldsymbol{\tau^{13}} &= \cos\Theta^{13}\sin\Theta^{23}\cos\Theta^{14}\cos\Theta^{34}\boldsymbol{\nabla}_R\Theta^{12} + \cos\Theta^{13}\cos\Theta^{23}\cos\Theta^{14}\sin\Theta^{24}\sin\Theta^{34}\boldsymbol{\nabla}_R\Theta^{12} - \cos\Theta^{23}\cos\Theta^{14}\cos\Theta^{34}\boldsymbol{\nabla}_R\Theta^{13} \\
&\quad + \sin\Theta^{23}\cos\Theta^{14}\sin\Theta^{24}\sin\Theta^{34}\boldsymbol{\nabla}_R\Theta^{13} \\
\boldsymbol{\tau^{23}} &= -\sin\Theta^{13}\cos\Theta^{24}\cos\Theta^{34}\boldsymbol{\nabla}_R\Theta^{12} - \cos\Theta^{13}\sin\Theta^{23}\sin\Theta^{14}\sin\Theta^{24}\cos\Theta^{34}\boldsymbol{\nabla}_R\Theta^{12} - \cos\Theta^{13}\cos\Theta^{23}\sin\Theta^{14}\sin\Theta^{34}\boldsymbol{\nabla}_R\Theta^{12} \\
&\quad + \cos\Theta^{23}\sin\Theta^{14}\sin\Theta^{24}\cos\Theta^{34}\boldsymbol{\nabla}_R\Theta^{13} - \sin\Theta^{23}\sin\Theta^{14}\sin\Theta^{34}\boldsymbol{\nabla}_R\Theta^{13} - \cos\Theta^{24}\cos\Theta^{34}\boldsymbol{\nabla}_R\Theta^{23} - \sin\Theta^{34}\boldsymbol{\nabla}_R\Theta^{24} \\
\boldsymbol{\tau^{14}} &= -\cos\Theta^{13}\sin\Theta^{23}\cos\Theta^{14}\sin\Theta^{34}\boldsymbol{\nabla}_R\Theta^{12} + \cos\Theta^{13}\cos\Theta^{23}\cos\Theta^{14}\sin\Theta^{24}\cos\Theta^{34}\boldsymbol{\nabla}_R\Theta^{12} + \cos\Theta^{23}\cos\Theta^{14}\sin\Theta^{34}\boldsymbol{\nabla}_R\Theta^{13} \\
&\quad + \sin\Theta^{23}\cos\Theta^{14}\sin\Theta^{24}\cos\Theta^{34}\boldsymbol{\nabla}_R\Theta^{13} - \cos\Theta^{24}\cos\Theta^{34}\boldsymbol{\nabla}_R\Theta^{14} \\
\boldsymbol{\tau^{24}} &= \sin\Theta^{13}\cos\Theta^{24}\sin\Theta^{34}\boldsymbol{\nabla}_R\Theta^{12} + \cos\Theta^{13}\sin\Theta^{23}\sin\Theta^{14}\sin\Theta^{24}\sin\Theta^{34}\boldsymbol{\nabla}_R\Theta^{12} - \cos\Theta^{13}\cos\Theta^{23}\sin\Theta^{14}\cos\Theta^{34}\boldsymbol{\nabla}_R\Theta^{12} \\
&\quad - \cos\Theta^{23}\sin\Theta^{14}\sin\Theta^{24}\sin\Theta^{34}\boldsymbol{\nabla}_R\Theta^{13} - \sin\Theta^{23}\sin\Theta^{14}\cos\Theta^{34}\boldsymbol{\nabla}_R\Theta^{13} + \cos\Theta^{24}\sin\Theta^{34}\boldsymbol{\nabla}_R\Theta^{23} - \cos\Theta^{34}\boldsymbol{\nabla}_R\Theta^{24} \\
\boldsymbol{\tau^{34}} &= -\sin\Theta^{13}\sin\Theta^{24}\boldsymbol{\nabla}_R\Theta^{12} + \cos\Theta^{13}\sin\Theta^{23}\sin\Theta^{14}\cos\Theta^{24}\boldsymbol{\nabla}_R\Theta^{12} - \cos\Theta^{23}\sin\Theta^{14}\cos\Theta^{24}\boldsymbol{\nabla}_R\Theta^{13} \\
&\quad - \sin\Theta^{24}\boldsymbol{\nabla}_R\Theta^{23} - \boldsymbol{\nabla}_R\Theta^{34}
\end{aligned}
$$

S4 Adiabatic Potential Energy Curves (PECs) and NACTs for TiO_6^{8-} unit of $BaTiO_3$ crystal

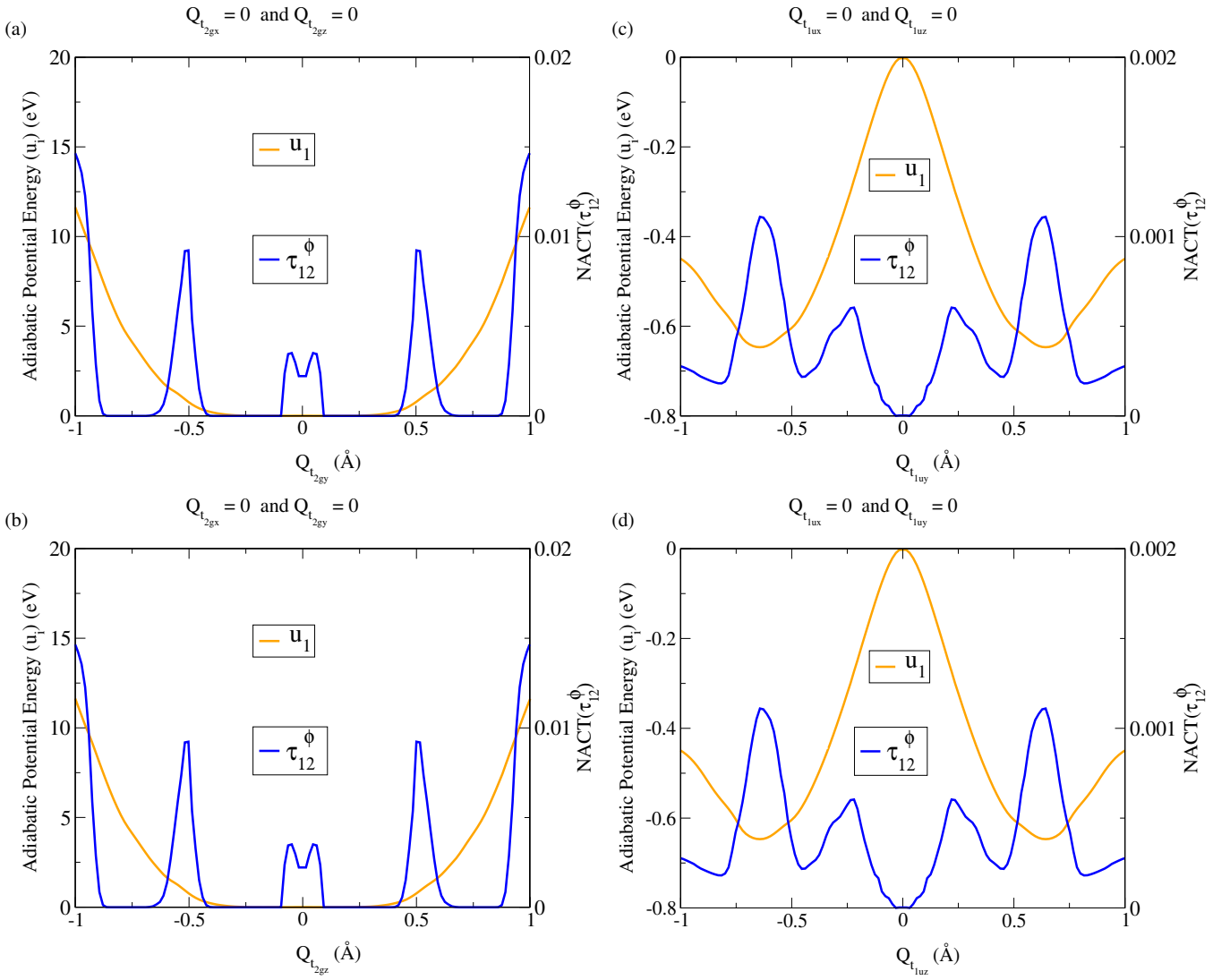

FIG. S1: For TiO_6^{8-} unit, 1D curves of lowest adiabatic PES (u_1) and the associated NACT (τ_{12}^{ϕ}) are presented along (a) $Q_{t_{2gy}}$, (b) $Q_{t_{2gz}}$, (c) $Q_{t_{1uy}}$, and (d) $Q_{t_{1uz}}$ normal modes keeping the other normal modes fixed at zero (0).

S5 Local Topographic Parameters and Adiabatic Potential Energy Surfaces Around the 2-3 Conical Intersection (CI)

We have calculated the local topographic parameter at the geometry of one of the '2-3' CI[5], where two independent geometrical distortions can linearly break the degeneracy, commonly known as *branching plane vectors*. These two vectors are mainly represented as $\vec{g}$ (the half-difference between the gradients of the two intersecting states) and $\vec{h}$ (the non-adiabatic coupling vectors between the two states). In order to calculate the local topographic parameters (tilt parameters (s_x and s_y), pitch of cone (d_{gh}) and asymmetry of cone (Δ_{gh})) for a double cone, we have employed COLUMBUS quantum chemistry package[6], where the calculated parameters are tabulated below:

s_x (eV/Å)	s_y (eV/Å)	Δ_{gh}	d_{gh} (eV/Å)
-0.046	-0.004	0.012	0.005

On the basis of above local topographic parameters, the model double cone adiabatic potential energy surfaces (PESs) have been calculated using the following functional form:

$$U_2 = s_x \cdot x + s_y \cdot y - d_{gh}\Big[\frac{x^2+y^2}{2} + \Delta_{gh}\frac{(x^2-y^2)}{2}\Big]^{1/2} \tag{S18}$$

$$U_3 = s_x \cdot x + s_y \cdot y + d_{gh}\Big[\frac{x^2+y^2}{2} + \Delta_{gh}\frac{(x^2-y^2)}{2}\Big]^{1/2} \tag{S19}$$

and the associated PESs are represented in the following figure:

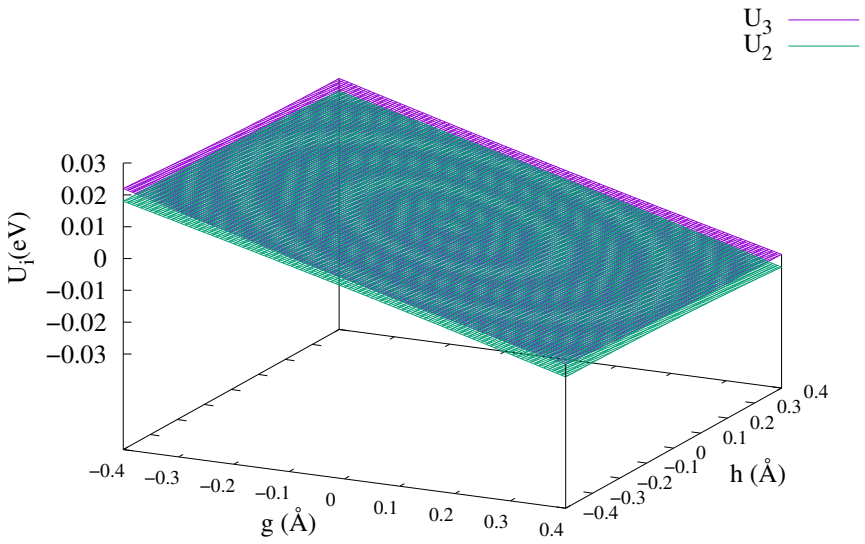

FIG. S2: Model adiabatic PESs around '2-3' CI along two branching plane vectors (g and h)

Figure S2 shows that the calculated model PESs using topographic parameters vary linearly at the close vicinity of CI. In other words, degeneracy is lifted linearly around the '2-3' CI indicating that the intersections are "conical" not glancing.

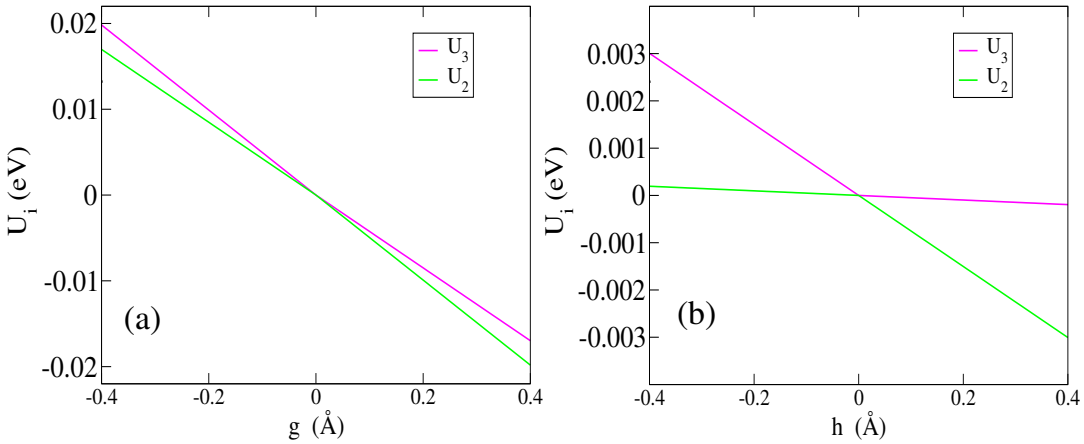

FIG. S3: 1D curves of model adiabatic PESs around '2-3' CI are presented along branching plane vector (a) g and (b) h. In each case, the PECs are plotted while keeping the other coordinate fixed at zero: (a) h = 0 and (b) g = 0.

S6 The t_{1u} normal mode vibration of TiO_6^{8-} unit

The triply degenerate vibrational modes (t_{1u}) are purely bending modes along XZ, XY and YZ plane. In *ab-initio* calculation, two modes are chosen along X and Y direction to locate the PJT minima.

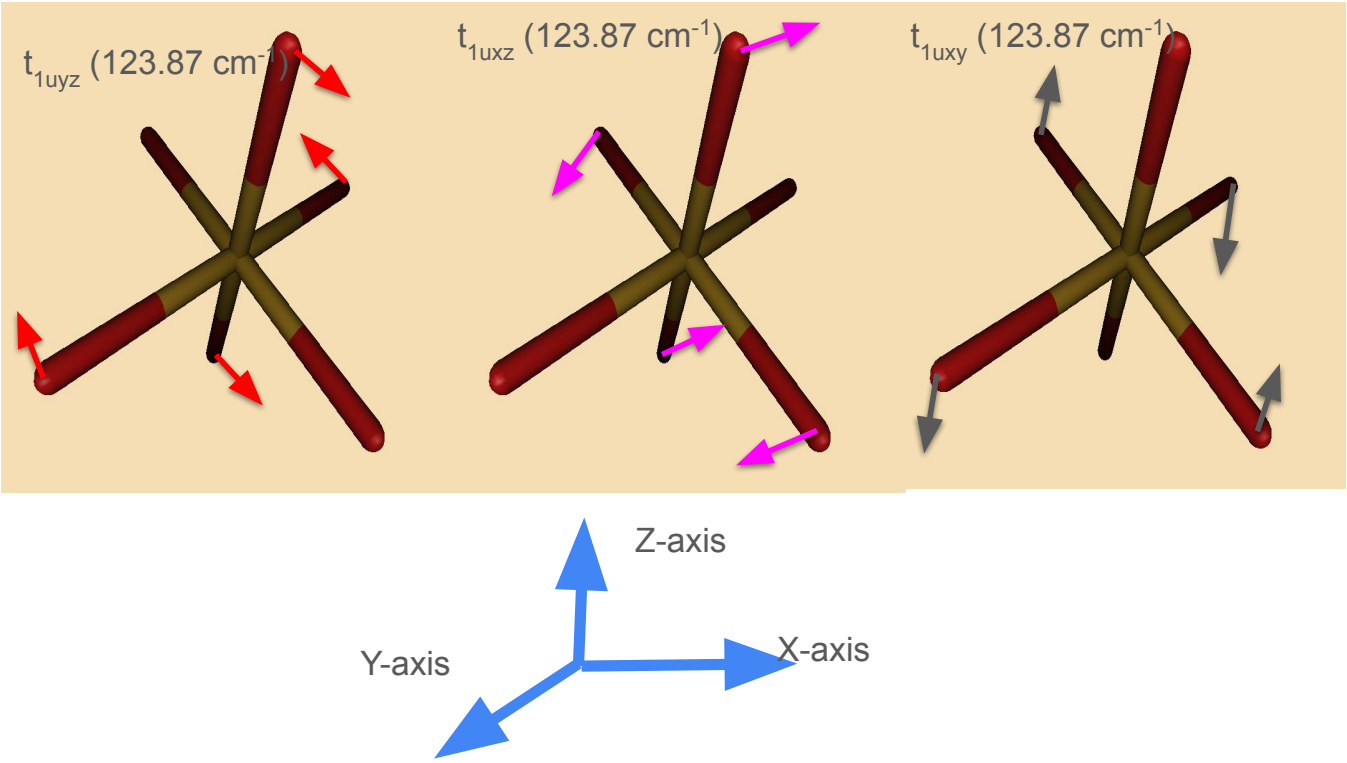

FIG. S4: Schemetic picture of t_{1u} modes of TiO_6^{8-} calculated at CCSD level for O_h configuration (Ti-O = 2.0 Å). The calculated frequency is 123.87 cm^{-1}. The arrow shows the bending motion of Ti-O bond.

S7 Optimized Geometry of TiO_6^{8-} on the ground state

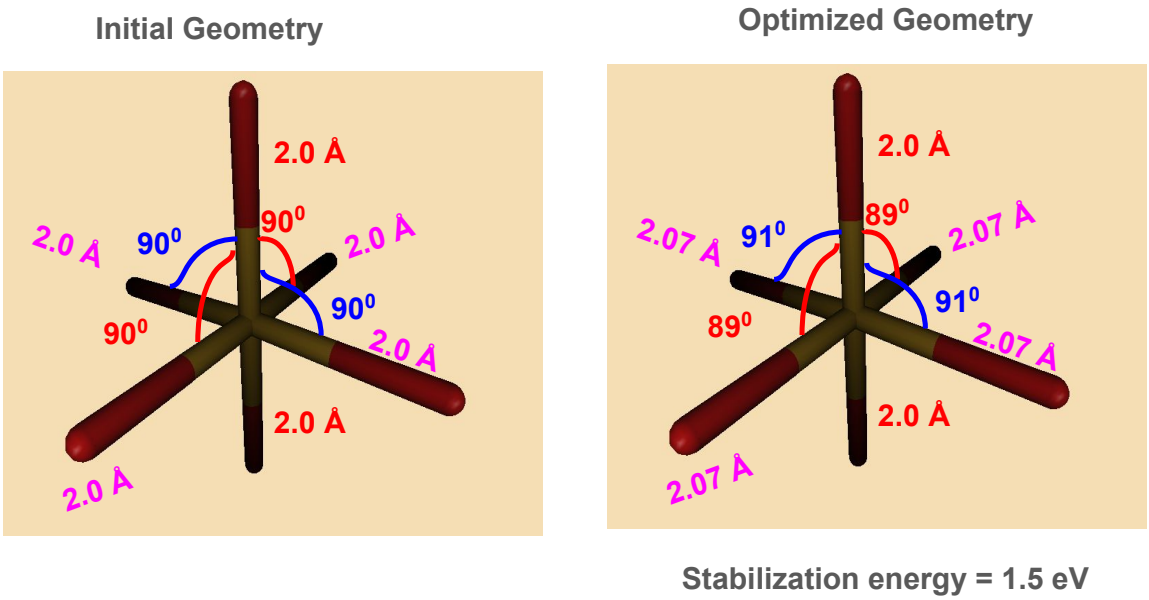

FIG. S5: The optimized geometry of TiO_6^{8-} on the ground state.

S8 Geometry of PJT Stabilized TiO_6^{8-} on the ground state

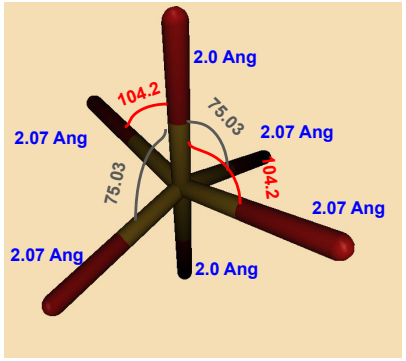

FIG. S6: The geometry of PJT stabilized TiO_6^{8-} on the ground state (extracted from *ab-initio calculation* at $\rho = 8.2$ and $\phi = 0$).

S9 Integration Paths for Stiff Differential Equations[7]

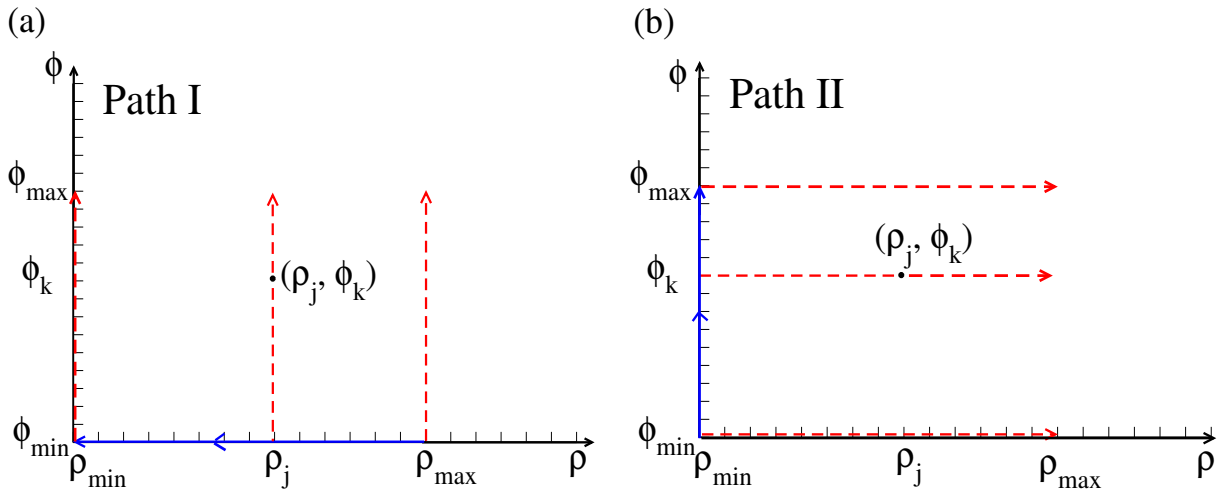

FIG. S7: Panels (a) and (b) depict the numerical solution of the stiff differential equations along path I and path II. The integration process involves solving the equations first along the bold (blue) line and subsequently along the dotted (red) lines in each case.

S10 An Overview on Time-Dependent Discrete Variable Representation (TDDVR) Formalism

The TDDVR formalism has been implemented over wide range of problems involving nuclear dynamics on low-dimensional model[8,9] systems as well as multi-dimensional multi-surface chemical processes[10–13]. While dealing with TDDVR dynamics in multi-dimensional multi-surface molecular systems, we can formulate the time-dependent Schrödinger Equation (TDSE) within the diabatic framework in the following manner,

$$i\hbar\frac{\partial}{\partial t}\Xi(\{Q_k\},t) = [\widehat{\mathbf{T}}_{nuc}\{Q_k\} + \hat{\mathbf{W}}(\{Q_k\})]\Xi(\{Q_k\},t), \tag{S20}$$

where $\hat{\mathbf{T}}_{nuc}\{Q_k\}$ ($= \hat{T}_{nuc}\{Q_k\}\cdot\mathbf{I}$) and $\hat{\mathbf{W}}(\{Q_k\})$ denote the kinetic energy operator and diabatic PES matrix, respectively, let say, expressed in terms of normal mode coordinates, $\{Q_k\}$. For systems

with N coupled electronic states, the nuclear wavefunction can be represented as follows,

$$\Xi(\{Q_k\},t) \equiv \begin{pmatrix} \psi_1(\{Q_k\},t) \\ \psi_2(\{Q_k\},t) \\ \psi_3(\{Q_k\},t) \\ \vdots \\ \psi_N(\{Q_k\},t) \end{pmatrix} \tag{S21}$$

where $\Xi(\{Q_k\},t)$ is normalized $[\int \Xi^{\dagger}(\{Q_k\},t)\Xi(\{Q_k\},t)\prod_{k=1}^{p} dQ_k = 1]$ at any time t.

In TDDVR formalism, the wavefunction corresponding to the l^{th} PES, denoted as $\psi_l(\{Q_k\},t)$ (see Eq. S21) is represented using TDDVR basis functions ($\chi_{i_k}(Q_k,t)$) for a total of p normal modes.

$$\psi_l(\{Q_k\},t) = \sum_{i_1 i_2 \ldots i_p} c_{i_1 i_2 \ldots i_p, l}(t) \prod_{k=1}^{p} \chi_{i_k}(Q_k,t) \tag{S22}$$

Alternatively, the TDDVR basis functions can be written in terms of Discrete Variable Representation (DVR) basis and time-evolving plane waves:

$$\chi_{i_k}(Q_k,t) = \phi(Q_k,t) \sum_{n=0}^{N_k} \zeta_n^*(x_{i_k})\zeta_n(x_k) \tag{S23}$$

$$= \sum_{n=0}^{N_k} \zeta_n^*(x_{i_k})\Phi_n(Q_k,t), \tag{S24}$$

where the plane wave takes the following form:

$$\phi(Q_k,t) = \pi^{1/4} \exp\left(\frac{i}{\hbar}\{p_{Q_k^c}(t)[Q_k - Q_k^c(t)]\}\right). \tag{S25}$$

In the DVR basis functions, harmonic oscillator eigenfunctions are chosen as the primitive bases (Eq. S23),

$$\zeta_n(x_k) = \left(\frac{2ImA_k}{\pi\hbar}\right)^{1/4} \frac{1}{\sqrt{n!2^n\sqrt{\pi}}} \exp\{-(x_k)^2/2\} H_n(x_k), \tag{S26}$$

where

$$x_k = \sqrt{\frac{2ImA_k}{\hbar}}(Q_k - Q_k^c(t)). \tag{S27}$$

In a similar way, the roots of $N_{k^{th}}$ Hermite polynomial, $H_{N_k}(x_k)$[14] attain the following expression,

$$x_{i_k} = \sqrt{\frac{2ImA_k}{\hbar}}(Q_{i_k}(t) - Q_k^c(t)), \tag{S28}$$

resulting into the following expression of TDDVR grid-points:

$$Q_{i_k}(t) = Q_k^c(t) + \sqrt{\frac{\hbar}{2ImA_k}} x_{i_k}. \tag{S29}$$

It's important to note that while the centre of the wavepacket ($\{Q_k^c\}$) and its momentum ($\{p_{Q_k^c}\}$) are assumed to be time-varying, the imaginary part of the width (ImA_k) is introduced as time-independent.[15] In simpler terms, the time dependency arises from the TDDVR grid points, Q_{i_k}s, which are influenced by the variables, $Q_k^c(t)$ and $p_{Q_k^c}(t)$.

The Gauss-Hermite (G-H) basis functions for the k^{th} normal mode ($\Phi_n(Q_k, t)$ in Eq. S24) are confirmed to be orthonormal[16], with the ground state representing the Gaussian Wave Packet (GWP). Similarly, the TDDVR basis functions χ_{i_k}s in Eq. (S23) for the k^{th} mode adhere to orthogonality, although they do not constitute a normalized set[16].

By substituting the TDDVR representation of wavefunctions (Eqs. S21 - S28) in the TDSE (Eq. S20), we get the following form of TDDVR matrix equation for the l^{th} PES,

$$i\hbar \mathbf{A}\dot{\mathbf{C}}_\mathbf{l} = \mathbf{H}^\mathbf{t}_\mathbf{ll}\mathbf{C}_\mathbf{l} + \mathbf{A}\sum_{\mathbf{l'}\neq\mathbf{l}} \mathbf{W}_\mathbf{ll'}\mathbf{C}_\mathbf{l'} \tag{S30}$$

which can be transformed into the following convenient (symmetric) form through a similarity transformation,

$$i\hbar \dot{\mathbf{D}}_\mathbf{l}(\mathbf{t}) = \mathbf{A^{-1/2}}\mathbf{H}^\mathbf{t}_\mathbf{ll}\mathbf{A^{-1/2}}\mathbf{D}_\mathbf{l} + \sum_{\mathbf{l'}\neq\mathbf{l}} \mathbf{W}_\mathbf{ll'}\mathbf{D}_\mathbf{l'} \tag{S31}$$

where $\mathbf{D_l} = \mathbf{A^{1/2}C_l}$. The detailed expression of the TDDVR coefficients, $d_{i_1 i_2 \ldots i_p, l}$ and the specific forms of various component matrices $\{\mathbf{X^k}\}$ and $\{\mathbf{Y^k}\}$) of $\mathbf{H^t}$ are provided in our earlier articles[16–18]. On the other hand, the center of the wavepacket ($\{Q_k^c\}$) and its momentum ($\{p_{Q_k^c}\}$) for the k^{th} mode involve the following classical equations of motion (EOMs):

$$\dot{Q}_k^c(t) = \frac{p_{Q_k^c}(t)}{\mu}, \tag{S32}$$

$$\dot{p}_{Q_k^c}(t) = -\frac{dW(\{Q_k\})}{dQ_k}\Big|_{Q_k(t)=Q_k^c(t)}. \tag{S33}$$

While deriving a first principle based explicit expression of $\dot{p}_{Q_k^c}$ for multi-dimensional multi-surface systems, it is necessary to employ the Dirac-Frenkel variational principle.[16–19] Interested readers

may refer to the aforementioned works for a thorough explanation of the initialization of wavepackets and their subsequent propagation over the diabatic PESs.

S11 Convergence Test of TDDVR Basis Set for Spectral Profile

In this present work, while performing the dynamics and calculating the PE spectra of the titanate (TiO_6^{9-}) system, we have optimized the basis functions, starting with smaller one, such as (3,3,3,3,3,3) [729 grid points] and then, going to the larger sets, such as (15,15,15,15,15,15) [1,13,90,625 grid points], to find the best combination for accurate calculations in TDDVR dynamics. In the above sets, the sequence of grid points represents six modes (t_{2g} and t_{1u} normal modes) of fundamental vibrational frequencies. On the process of the convergence analysis to obtain the converged spectral profiles for combined four states (A_{1g} and T_{1u}) (13,7,7,13,11,11), total 10,02,001 number of grid points are involved. In order to explore such convergence, four representative PE spectra are shown in the Figure S8.

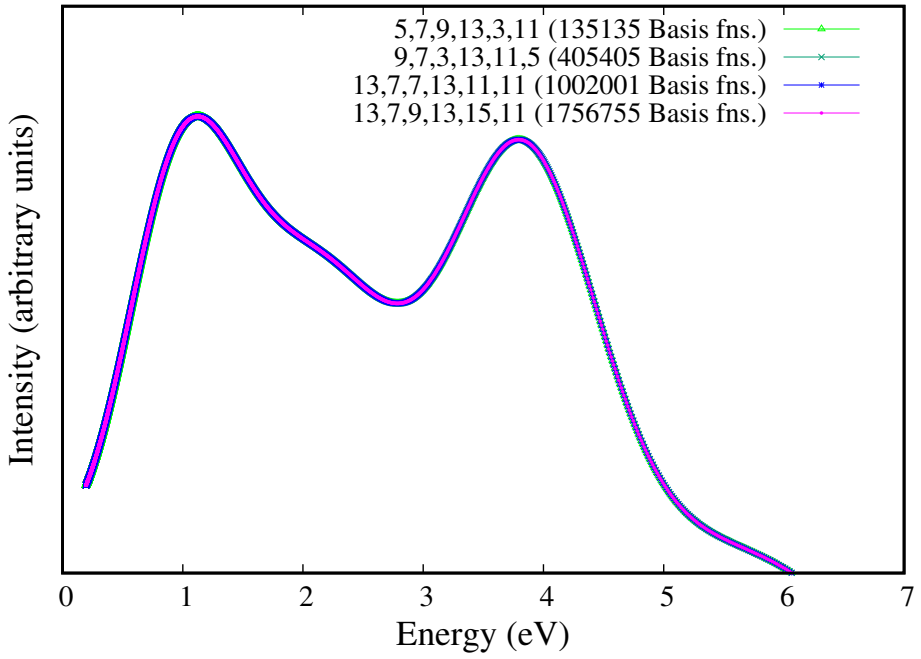

FIG. S8: TDDVR calculated spectra obtained from BBO based diabatic PESs are presented for four sets of basis functions. All sets are almost superimposed with each other and therefore, the set 13,7,7,13,11,11 is used as the optimized set of basis function.

S12 Theoretical and Experimental: Spontaneous Polarization vs Temperature

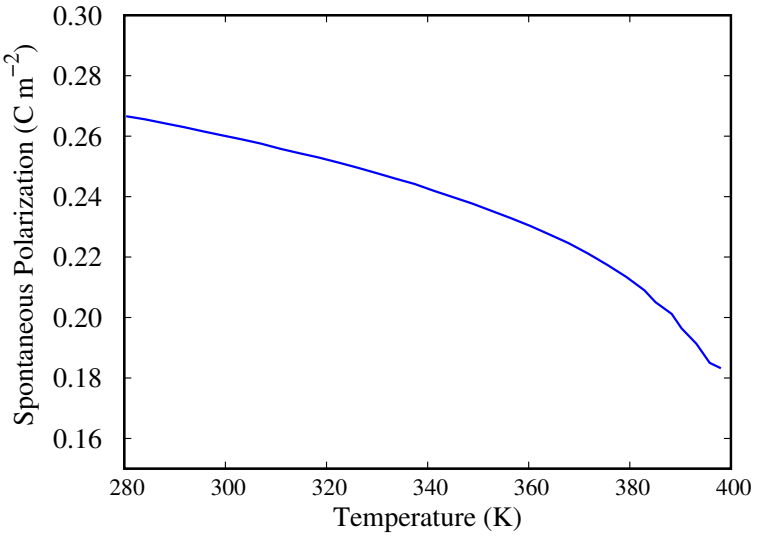

FIG. S9: Dependence of polarization on temperature for $BaTiO_3$ single crystal for tetragonal to cubic phase by Li *et al.*[20].

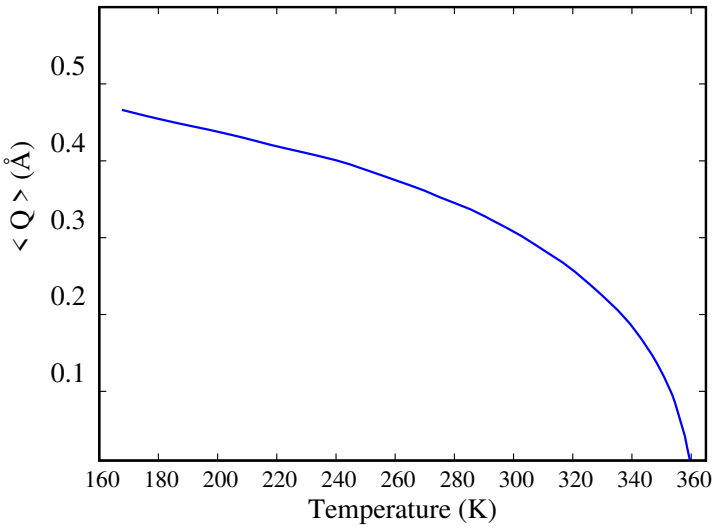

FIG. S10: Temperature dependence of the order parameter $\langle Q \rangle$ (in Å) from tetragonal to cubic phase by V. Polinger[21].

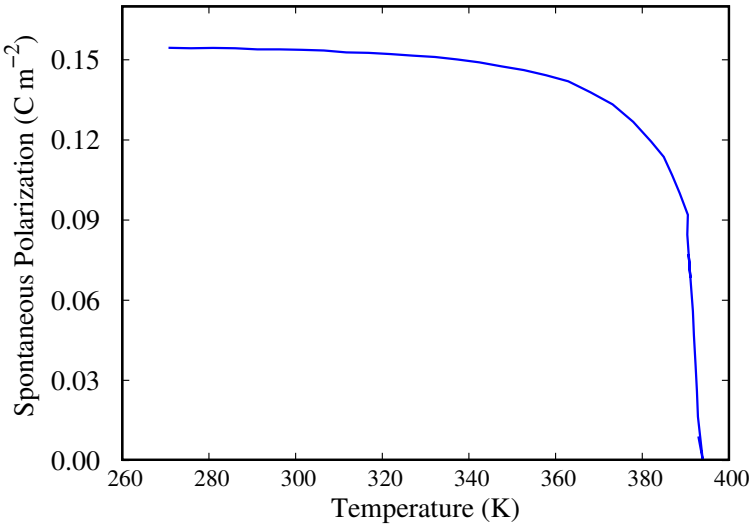

FIG. S11: Spontaneous polarization as a function of temperature for tetragonal to cubic phase by Walter J. Merz[22].

References

[1] I. B. Bersuker, *Appl. Phys. Lett.*, 2015, **106**, 022903.

[2] R. Baer, D. M. Charutz, R. Kosloff and M. Baer, *J. Chem. Phys.*, 1996, **105**, 9141.

[3] M. K. Sah, S. Mukherjee, K. Naskar, S. Hazra and S. Adhikari, *Int. J. Quantum Chem.*, 2023, **123**, e27212.

[4] B. Sarkar and S. Adhikari, *J. Phys. Chem. A*, 2008, **112**, 9868–85.

[5] D. R. Yarkony, *J. Chem. Phys.*, 2001, **114**, 2601–2613.

[6] M. Barbatti, A. J. A. Aquino and H. Lischka, *J. Phys. Chem. A*, 2005, **109**, 5168–5175.

[7] M. K. Sah, S. Mukherjee, S. Saha, K. Naskar and S. Adhikari, *J. Chem. Phys.*, 2023, **159**, 244116.

[8] S. Sardar, A. K. Paul and S. Adhikari, *J. Chem. Sc.*, 2010, **122**, 491.

[9] S. Sardar, A. K. Paul and S. Adhikari, *Mol. Phys.*, 2009, **107**, 2467.

[10] S. Sardar, A. K. Paul, R. Sharma and S. Adhikari, *Int. J. Quantum Chem.*, 2011, **111**, 2741–59.

[11] S. Sardar, A. K. Paul, R. Sharma and S. Adhikari, *J. Chem. Phys.*, 2009, **130**, 144302.

[12] S. Sardar and S. Adhikari, *J. Chem. Sci.*, 2012, **124**, 51–8.

[13] B. A. Khan, S. Sardar, P. Sarkar and S. Adhikari, *J. Phys. Chem. A*, 2014, **118 (49)**, 11451.

[14] G. D. Billing and S. Adhikari, *Chem. Phys. Lett.*, 2000, **321**, 197.

[15] B. Barkakaty and S. Adhikari, *J. Chem. Phys.*, 2003, **118**, 5302.

[16] S. Mandal, S. Ghosh, S. Sardar and S. Adhikari, *Int. Rev. Phys. Chem.*, 2019, **37**, 607–700.

[17] S. Mukherjee, S. Ravi, K. Naskar, S. Sardar and S. Adhikari, *J. Chem. Phys.*, 2021, **154**, 094306.

[18] S. Mukherjee, S. Ravi, J. Dutta, S. Sardar and S. Adhikari, *Phys. Chem. Chem. Phys.*, 2022, **24**, 2185–2202.

[19] P. A. M. Dirac, *Proc. Cambridge philos. Soc.*, 1930, **26**, 376.

[20] Y. L. Li, L. E. Cross and L. Q. Chen, *J. Appl. Phys.*, 2005, **98**, 064101.

[21] V. Polinger, *J. Phys.: Conf. Ser.*, 2013, **428**, 012026.

[22] W. J. Merz, *Phys. Rev.*, 1949, **76**, 1221–1225.